Smart Materials and Structures

PAPER

Development and fault-tolerant control of a distributed piezoelectric stack actuator

To cite this article: Yunzhi Zhang *et al* 2024 *Smart Mater. Struct.* **33** 095003

IOP Publishing Smart Materials and Structures
Smart Mater. Struct. **33** (2024) 095003 (15pp) https://doi.org/10.1088/1361-665X/ad669e

Development and fault-tolerant control of a distributed piezoelectric stack actuator

Yunzhi Zhang, Jie Ling* and Yuchuan Zhu

College of Mechanical and Electrical Engineering, Nanjing University of Aeronautics and Astronautics, Nanjing 210016, People's Republic of China

E-mail: meejling@nuaa.edu.cn

Received 31 May 2024, revised 10 July 2024
Accepted for publication 23 July 2024
Published 1 August 2024

Abstract

Piezoelectric stack actuator (PSA) has attracted widespread attention in aerospace applications. However, the severe operating conditions would bring certain risks to PSA, leading to decreased performance or even failure. The conventional PSA structure lacks adaptability in the event of a complete failure occurring within the piezoelectric stack layer (PSL) due to its centralized design and driving method. To address the reliability challenges inherent in PSAs, this paper proposes a novel distributed PSA (DPSA) by means of mechanical and electrical dispersion. Additionally, dual-redundant PSLs are integrated into the DPSA as backups, providing hardware redundancy for active fault-tolerant control (FTC). Building upon this foundation, an sliding mode observer (SMO)-based fault detector for DPSA is developed to facilitate fault reconstruction. Subsequently, an active FTC strategy, comprising dual-SMO-based fault detectors and a tracking controller, is introduced to effectively manage faults and reallocate control resources. Comprehensive experiments under various fault scenarios are carried out to assess the performance of the SMO-based fault detector and FTC strategy. The results demonstrate that the proposed fault detector and FTC strategy promptly detect faults and efficiently restore the DPSA to a stable state, thereby ensuring effective trajectory tracking even in the presence of faults.

Keywords: piezoelectric stack, distributed structure, fault detection, fault-tolerant control, high reliability

Nomenclature

PEA:	Piezoelectric actuator.
FTC:	Fault-tolerant control.
SMO:	Sliding mode observer.
PSA:	Piezoelectric stack actuator.
PSL:	Piezoelectric stack actuator layer.
DPSA:	Distributed piezoelectric stack actuator.

* Author to whom any correspondence should be addressed.

1. Introduction

With the advantages of high resolutions, fast response, and compact structure [1, 2], PEAs have attracted widespread attention in aerospace electro-hydraulic systems for high-speed and high-precision fluid power transmission and control [3, 4]. In such systems, PEAs have been studied to serve as the core actuating parts of the fluid control or power components, such as flow control valves [5, 6], digital on/off valves [7, 8], and hydraulic pumps [4, 9].

However, the severe operating conditions in aerospace applications would bring certain risks to PEAs, leading to

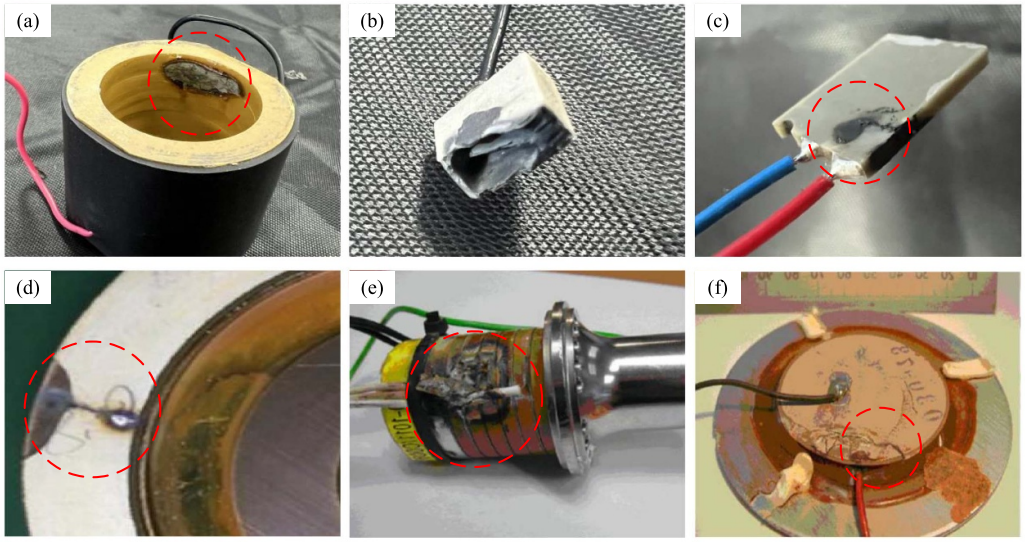

Figure 1. Conditions of PEA failure. Cases from authors' Lab: (a) failure of the ring piezoelectric stack; (b) complete breakdown of the piezoelectric stack; (c) failure of the bimorph-type PEA. Cases from literature: (d) crack of the PEA in the ultrasonic motor; (e) complete breakdown of the piezoelectric stack [15]; (f) crack of the piezoelectric-actuated acoustic device [15];.

decreased performance or even complete failure, which limits their application in this field. The following provides a detailed introduction to the reliability research of PEAs under extreme working conditions. When the PEAs are used to drive the fuel injectors or fuel modulation valve, the surrounding temperature ranges from −40 °C to 120 °C [10]. Due mainly to thermal depolarization (reduction of remnant polarization), the performance of PEAs always fluctuates and eventually deteriorates at high temperatures even far below curie temperature [11]. High temperatures will also accelerate the fatigue failure of piezoelectric materials [12]. Low surrounding temperatures would cause partial microcracks of the piezoelectric materials to propagate [13]. In addition, operating under high electric-field magnitudes and/or high frequency will cause the self-heat in PEAs [14, 15]. The heat may significantly affect the lifetime, durability, positioning accuracy of the actuators, and degradation of the material properties [10, 16]. Furthermore, long-time operating will cause internal localized overheating which brings damage to the PEAs. Specifically, in aerospace applications, thermal-induced failure of PEAs includes as follows:

(1) Extremely high or low surrounding temperature can cause fatigue damage to the piezoelectric material, while increased temperature further accelerates the rate of fatigue damage.
(2) Continuous long-time actuation under high electric-field magnitudes and/or high frequency generates self-heat in the piezoelectric, which can result in local overheating, leading to failure.

From the perspective of structure and working principles, conventional stack-type or bimorph-type PEAs only have a pair of positive and negative terminals, known as a 'centralized structure'. Although the centralized structure and driving method have the advantage of system simplicity, the damage occurring to a single piezoelectric layer will lead to the overall failure of the actuator, resulting in lower reliability. Here are some examples of the PEA breakdown condition in figure 1. Hence, it is necessary to modify the structure and driving method of the PEAs. Meanwhile, considering enhancing the PEAs' reliability with severe operating conditions, there is a great need to study the FTC on PEAs. Generally speaking, FTC can be divided into two categories: (1) passive FTC and (2) active FTC [17]. The passive FTC does not depend on fault information and mainly explores the robustness of the underlying controller. On the contrary, active FTC reacts when a fault occurs and the controller would be reconfigured with the help of the information derived from the fault detector. This represents a more flexible structure and is robust when faced with serious failures, such as a general actuator/sensor failure.

To design the active FTC, the fault detector is the primary focus. The fault detection methods include (1) model-based method and (2) model-free method (signal processing method or data-driven method) [18, 19]. Conventional model-based fault detector is composed of a residual generator, an evaluation function and a detection logic with a threshold [20]. With the threshold and the residual signal, the fault detector can judge whether the fault occurs or not. However, this method imposes a high demand on threshold design. As working conditions change, the threshold often requires revision, posing significant challenges for fault detector design. Meanwhile, given the influence of system disturbances, this method can easily lead to misdiagnoses. To enhance the fault detector's performance, fault reconstruction methods are proposed with the observers. The observer obtains the internal state information of the system by estimating the state variables to track the fault, judge the type of the fault, and provide the basis

for eliminating the impact of the fault on the system [17]. Sliding mode techniques have good robustness and are completely insensitive to uncertainty [21, 22], which can be used to design the observer. Sreedhar *et al* [23] first proposed a SMO for fault detector in 1993 realizing a robust detection of a subset of sensor, actuator, and process faults. Tan and Edwards [24] proposed a fault detector scheme with SMO and linear matrix inequalities (LMI) for linear systems with uncertainty. Based on these, to realize the fault reconstruction of nonlinear systems, Yan and Edwards [25] designed an SMO that accomplished fault reconstruction for nonlinear systems satisfying the Lipschitz condition. Moreover, some applications concerned with the use of SMO for fault detection and reconstruction have been discussed in several papers recently [26–29]. Thanks to lots of work on PEA's modeling in academia [30, 31], the SMO methods have been used in state estimation of PEAs considering unmodelled errors or disturbances [32, 33]. However, to the best of our knowledge, little work in the literature focuses on fault modeling and reconstruction of PEAs. Since the SMO seems to be suitable for PEAs' fault detector design to estimate the fault signal and the inherent hysteresis nonlinear of PEAs can be modeled with the hysteresis model, it has the potential to simplify the SMO design and stability proof without the traditional way with Lipschitz functions [34, 35].

Another aspect of designing active FTC involves configuring redundant resources as backup plans to enhance the system's reliability, availability, and fault tolerance. The redundant resources include (1) hardware redundancy; and (2) analytical redundancy [17]. The case that redundant actuators /sensors are added to the system as backups is hardware redundancy. Hardware redundancy is commonly used in situations where safety requirements are very high, such as in aircraft [36]. Analytical redundancy, as described above, is a type of observer running as a mathematical model or algorithm in a computer. It can replace the function of sensors without the need for additional hardware, thereby reducing weight and cost. With the fault detector information from the observers and the redundant actuators/sensors, the control force can be reallocated to realize the FTC. To the best of our knowledge, little work in the literature focuses on redundant design, fault detection, and FTC of PEAs themselves.

Hence, the main motivation of this work is to design a new PSA structure with redundant PSLs and then to develop the fault detector and FTC design corresponding to the new structure, thus finally improving the reliability of PSA. The novelties of the work include as follows:

(1) A DPSA structure design with novel distributed working methods and redundant PSLs.
(2) Mathematical modeling of DPSA with fault and SMO-based fault detector design for fault reconstruction.
(3) FTC strategy with dual-fault detectors for DPSA's fault management and control force reallocation to redundant PSLs.

The remainder of this paper is organized as follows. Section 2 presents the structure and working principle of the proposed DPSA. Meanwhile, the experiment platform of the proposed DPSA is illustrated in this section. The mathematical model of the DPEA with fault is carried out in section 3 and the fault detector with SMO for DPSA is designed based on the model. In section 4, the FTC is designed based on the DPSA and fault detector with SMO. In section 5, a series of experiments of the proposed fault detector and FTC are conducted. In section 6, some discussions of the experimental results are made. Conclusions are drawn in section 7.

2. Structure and working principle

2.1. Structure and construction of the distributed PSA

In contrast to the conventional PSA, each PSL of the DPSA is mechanically bonded and electrically shares a pair of positive and negative terminal poles (actuated centrally), DPSA adopts a distributed piezoelectric stack as the core driving component. The structure and construction of the proposed DPSA are shown in figure 2.

In this approach, each PSL is kept separate from the others, with interlayers placed between PSLs, which realizes the mechanical dispersion. The interlayers are insulating films with two functions: (1) prevent the electrodes of two piezoelectric stacks from contacting each other; (2) when a PSL experiences breakdown failure, the unaffected PSLs are protected from spark caused by breakdown. Meanwhile, two spare-PSLs, serving as redundant resources, are integrated into the DPSA for subsequent implementation of FTC.

With the help of interlayers, the driving electrodes of each PSL are independently controlled electrically. Furthermore, the amplifier is multiple-input-multiple-output so that the driving signal is independent of each other. With the FTC, the control force can be reallocated based on the fault detection results and each PSL can be decided to be actuated or not individually. Hence, the electrical dispersion is realized and FTC can be designed based on the dispersion.

2.2. Working principle of the distributed PSA under fault

The active FTC designed in this paper is aimed at the extreme case of complete failure of the PSA, which means both the electrodes and the PSA break down. The conventional piezoelectric stack and the distributed one's performance under fault are explained in figure 3. It can be seen that if the fault occurs, the displacement of the PEA will decrease and the PSL with fault will not output displacement forever. More seriously, each of the electrodes of the conventional piezoelectric stack will break down because of the fault, thus the conventional piezoelectric stack loses effect.

Thanks to the distributed structure, the DPSA will still output displacement because the electrodes of each PSL are separated. It improves the actuator's reliability. Since the maximum of each PSL's input voltage is restricted to avoid overload, the displacement of the actuator will be restricted. With the FTC and redundant PSLs, the fault can be detected by the fault

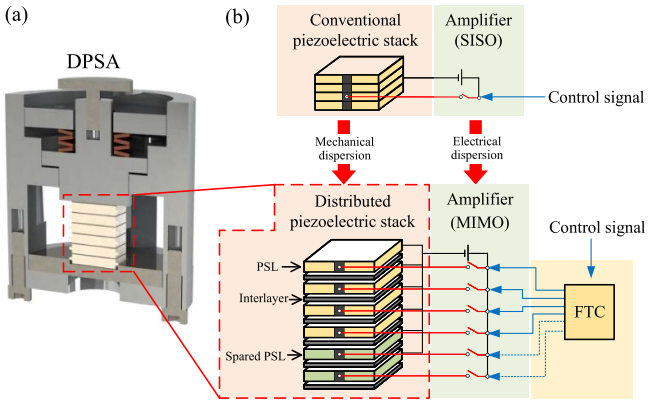

Figure 2. Structure and construction of the distributed piezoelectric stack actuator (DPSA). (a) Three-dimensional model of the DPSA. (b) Detailed illustration of the construction of distributed piezoelectric stack in comparison with the conventional one.

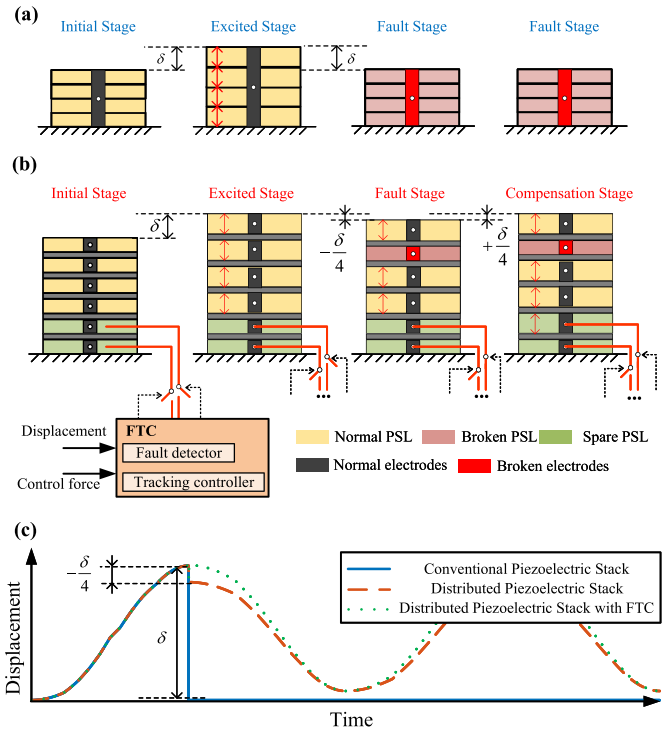

Figure 3. Comparison of the performance of the conventional PSA and the DPSA under fault. (a) Conventional piezoelectric stack working under fault. (b) Distributed piezoelectric stack working under fault. (c) Fault explanation with output displacement.

detector and it will reallocate the control force to the spare-PSL which serves as the backup of the faulty PSL to output displacement. Thus, the performance of the actuator can be guaranteed and it improves the actuator's reliability once again. With the structure design, the follow-up work is to complete the design of the fault detector and FTC.

2.3. Experimental platform of the distributed PSA

The experimental platform and signal flow diagram of DPSA are shown in figure 4. The controller adopts an xPC-Target real-time control system which is composed of two PCI-6259 motion acquisition cards, four interface boards, a host PC, and a target PC. The power amplifier is self-made with eight I/O channels. The DPSA adopts six layers (single layer thickness is 2 mm) of piezoelectric stacks (Harbin Core Tomorrow Science & Technology Co., Ltd NAC2015). The capacitive displacement sensor (Harbin Core Tomorrow Science & Technology Co., Ltd E09.Cap) collects the displacement of the actuator.

3. Fault detection method

3.1. Mathematical model with fault of the distributed PSA

For active FTC, the fault detector design is the first step. To design the observer-based fault detector, the state space model of the DPSA with fault needs to be built. Since the model of

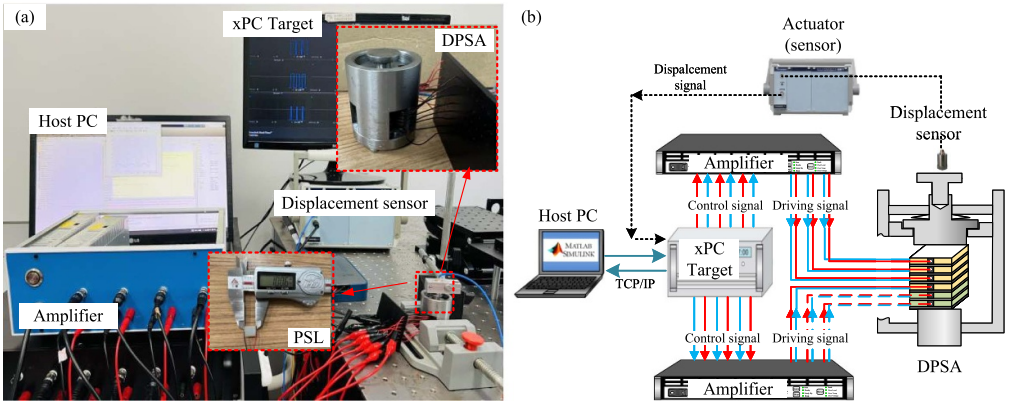

Figure 4. Experimental setup of the DPSA: (a) Experimental platform; (b) Block diagram of signal flow.

PSAs includes linear dynamics and hysteresis [37], the state space model with fault of the DPSA can be described as follows:

$$\begin{cases} \begin{pmatrix} \dot{z}_1 \\ \dot{z}_2 \end{pmatrix} = \underbrace{\begin{pmatrix} 0 & 1 \\ -\frac{k}{m} & -\frac{b}{m} \end{pmatrix}}_{A} \begin{pmatrix} z_1 \\ z_2 \end{pmatrix} + \left[\underbrace{\begin{pmatrix} 0 \\ \frac{kd}{m} \end{pmatrix}}_{B} u + \begin{pmatrix} 0 \\ -\frac{k}{m} \end{pmatrix} h \right] \\ \quad + \underbrace{\left[\begin{pmatrix} 0 \\ \frac{kd}{m} \end{pmatrix} \frac{u}{n} + \begin{pmatrix} 0 \\ -\frac{k}{m} \end{pmatrix} \frac{h}{n} \right]}_{G} \mathrm{f} + Dd(x,u,t) \\ y = \underbrace{\begin{pmatrix} 1 & 0 \\ 0 & 1 \end{pmatrix}}_{C} \begin{pmatrix} z_1 \\ z_2 \end{pmatrix} \end{cases} . \quad (1)$$

Here, $z_1 \in R$ is the output displacement of the DPSA, $z_2 = \dot{z}_1 \in R$ is the velocity of the DPSA, parameters m, b, k, and d represent the mass, damping coefficient, stiffness and piezoelectric coefficient. n is the number of the operational PSLs of the DPSA when no breakdown failure occurs. $D = \left(\begin{smallmatrix} 1 & 0 \\ 0 & 1 \end{smallmatrix}\right) \in R^{2\times 2}$ is the uncertainty matrix defined by the users. $d(x,u,t) \in R^{2\times 1}$ is the unknown bounded uncertainty. $u \in R$ denotes the input voltage, and $h \in R$ indicates the hysteresis which can be calculated by (2) and (4) [38]. $\mathrm{f} \in R$ is the opposite number of the number of breakdown PSLs when breakdown failure occurs. G is the fault distribution matrix which is calculated by the input signal u and hysteresis h, realizing the approximation to real failure conditions.

$$h[u](t) = w_0 u(t) + \sum_{i=1}^{n} w_i Hj_i[u](t), \quad i = 1,2,\ldots,n \quad (2)$$

where n represents the number of backlash operators, w_i means the weights of each operator, and j_i are positive thresholds which is calculated as follows,

$$j_i = \frac{i-1}{n_j} u_{\max}, \quad (3)$$

where n_j represents the number of thresholds and $u_{\max}$ is the maximum of the input voltage. Here the $u_{\max} = 100$.

Backlash operators H_{j_i} can be described in the following formula as,

$$Hj_i[u](t) = \max(u(t) - j_i, \min(u(t) + j_i, Hj_i[u](t - t_s))) \quad (4)$$

where t_s means the sampling period.

Hence, if no failure occurs, $\mathrm{f} = 0$. Without considering the unknown bounded uncertainty, the model in (1) will be simplified as the dynamic model of normal PSAs with hysteresis. The parameters of which can be identified off-line by open-loop tests with two steps:

(1) Identifying the linear dynamic parameters of the system through small step signals to reduce the influence of hysteresis nonlinearity.
(2) Identifying the parameters of the hysteresis models based on the identified linear dynamic parameters through the quasi-static harmonic signal.

The parameter identification is conducted in MATLAB and the cost function is set to minimize the sum squared error. The optimization method is Nonlinear least squares and the algorithm is trust-region-reflective. Based on the open-loop test data, the parameters of the model without fault are identified in table 1. It should be mentioned that it is the $\frac{kd}{m}$, $\frac{k}{m}$, $\frac{b}{m}$, w_i being identified for convenience of the fault detector with SMO design.

The model validation was shown in figure 5. It can be seen from the comparison between the experiment data and the model data that the mathematical model of DPSA without fault has the ability to describe the output characteristics. To quantify modeling errors, the root-mean-square (RMS) error and the relative RMS (RRMS) error are calculated in this paper. They are defined as follows:

$$e_{\mathrm{rms}} = \sqrt{1/T \int_0^T |x(t) - x_d(t)|^2 \, \mathrm{d}t} \quad (5)$$

Table 1. The identified parameters of the model.

Symbol	Value	Unit	Symbol	Value	Unit
$\frac{k}{m}$	8.2×10^{7}	$\mathrm{N\,(kg{\cdot}m)^{-1}}$	w_5	-0.014	—
$\frac{b}{m}$	1.4×10^{4}	$\mathrm{Ns\,(kg{\cdot}m)^{-1}}$	w_6	0.070	—
$\frac{kd}{m}$	2.9×10^{6}	$\mathrm{Ns\,(kg{\cdot}\mu m)^{-1}}$	w_7	-0.074	—
w_1	0.004	—	w_8	0.012	—
w_2	-0.027	—	w_9	0.007	—
w_3	-0.011	—	w_{10}	-0.037	—
w_4	-0.011	—	n_j	10	—

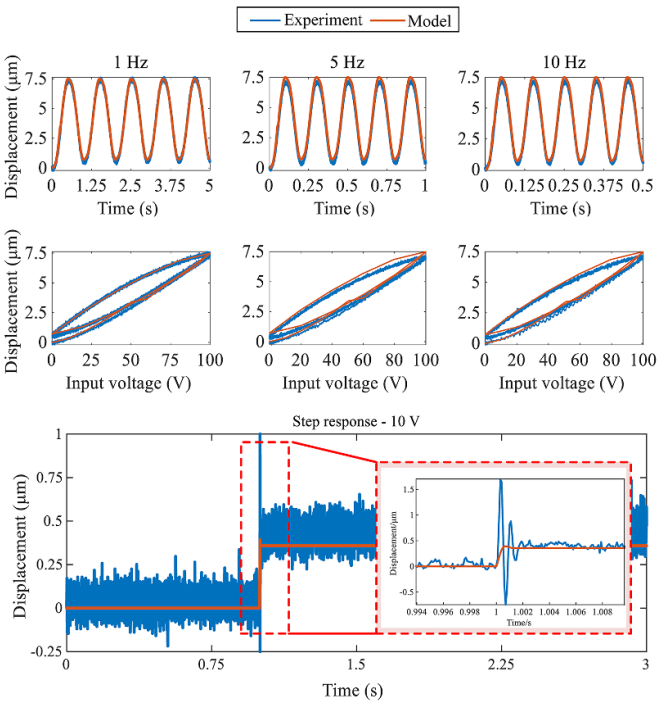

Figure 5. Verification of the dynamic model of DPSA under different input signals.

$$e_{\mathrm{rrms}}=\frac{e_{\mathrm{rms}}}{\max\left(x(t)\right)}\times100\%, \tag{6}$$

where $x(t)$ and $x_d(t)$ are the experimental and model displacements respectively, and T is the total time. The results show that: the RMS error (resp. RRMS error) at 1 Hz, 5 Hz, and 10 Hz is 0.012 μm (resp. 1.4%), 0.091 μm (resp. 4.2%), and 0.057 μm (resp. 3.2%). It can be seen that the mathematical model of DPSA without fault established has high accuracy within 10 Hz. The unmodeled error can be regarded as uncertainty $Dd(x,u,t)$, which can be restrained in the subsequent fault detection design.

3.2. SMO design for fault detection

The state observer for the system shown in (1) is designed using the Edwards–Spurgeon observer design method [22], shown in (7)

$$\begin{cases}\begin{pmatrix}\dot{\hat{z}}_1\\ \dot{\hat{z}}_2\end{pmatrix}=(A-LC)\begin{pmatrix}\hat{z}_1\\ \hat{z}_2\end{pmatrix}+Ly+Bu+\begin{pmatrix}0\\ -\frac{k}{m}\end{pmatrix}h+G\hat{\mathrm{f}}+Dv\\ \hat{y}=C\begin{pmatrix}\hat{z}_1\\ \hat{z}_2\end{pmatrix}\end{cases} \tag{7}$$

where the matrix $A\in R^{2\times2}$, $B\in R^{2\times1}$,$C\in R^{2\times2}$ are known matrices. $L\in R^{2\times1}$ is the observer gain matrix, which needs to be designed. $G\in R^{2\times1}$ is the fault distribution matrix, according to (1), G is known if u is known. $\hat{z}_1$ and $\hat{z}_2$ are the estimated state vector by the observer. Different from the existing methods that the nonlinear part is treated as a bounded unknown function satisfying the Lipschitz condition, the hysteresis model h calculated by (2) is applied to the SMO to replace the bounded unknown nonlinear function. The parameters of h are identified offline so that h is only related to the input signal u and does not need to be estimated. $v\in R^{2\times1}$ is a discontinuous term defined as follows:

$$v=\begin{cases}-\rho\frac{Fe}{\|Fe\|+\delta} & \text{if} \quad e\neq0\\ 0 & \text{if} \quad e=0\end{cases} \tag{8}$$

where $e=\hat{z}-z$ is defined as the error vector between the estimated state vector with the actual one, δ is a scalar with a small value to avoid the discontinuous control brings oscillations to the system as well as high-frequency disturbances caused by these oscillations. ρ and F are the parameters designed by the users. Then the function of the observer error is as follows:

$$\dot{e}(t)=(A-LC)e(t)+G\tilde{\mathrm{f}}+D\left(v-d(x,u,t)\right) \tag{9}$$

where $\tilde{\mathrm{f}}=\hat{\mathrm{f}}-\mathrm{f}$ is defined as the error between the estimated fault with the actual fault. To facilitate the SMO, the following assumptions are imposed with respect to the system (4).

Assumption 1. The matrix pair (A,C) is detectable. This means there exists a matrix $A_0=A-LC\in R^{2\times2}$ and the real part of the eigenvalues of A_0 is less than 0.

Assumption 2. There exists two positive definite symmetric matrices $Q\in R^{2\times2}$ and $P\in R^{2\times2}$, which satisfy the Lyapunov equation:

$$A_0^TP+PA_0=-Q \tag{10}$$

has an unique solution $P>0$.

Assumption 3. $\mathrm{rank}(CG)=\mathrm{rank}(G)$

Assumption 4. There exists a positive function ρ, such that $\|d(x,u,t)\| \leqslant \rho$

From the principles of SMO design, the following lemma can be derived [26] as follows:

Lemma 1. *If there exists P_0 and P, which are positive definite and symmetric, on the basis of assumptions 1∼4, the fault reconstruction law is as follows:*

$$\hat{\dot{f}} = -P_0^{-1} G^{\mathrm{T}} P e \tag{11}$$

Then,

$$\lim_{t\to\infty} e(t) = 0, \lim_{t\to\infty} \tilde{f}(t) = 0 \tag{12}$$

Proof. Choose the Lyapunov function:

$$\begin{aligned}
V &= e^{\mathrm{T}} P e + \tilde{\mathrm{f}}^{\mathrm{T}} P_0 \tilde{\mathrm{f}} \\
\dot{V} &= \dot{e}^{\mathrm{T}} P e + e^{\mathrm{T}} P \dot{e} + \tilde{\dot{\mathrm{f}}}^{\mathrm{T}} P_0 \tilde{\mathrm{f}} + \tilde{\mathrm{f}}^{\mathrm{T}} P_0 \tilde{\dot{\mathrm{f}}} \\
&= e^{\mathrm{T}} A_0^{\mathrm{T}} P e + \tilde{\mathrm{f}}^{\mathrm{T}} G^{\mathrm{T}} P e + (v - d(x,u,t))^{\mathrm{T}} D^{\mathrm{T}} P e + e^{\mathrm{T}} P A_0 e \\
&\quad + e^{\mathrm{T}} P G \tilde{\mathrm{f}} + e^{\mathrm{T}} P D (v - d(x,u,t)) + \tilde{\dot{\mathrm{f}}}^{\mathrm{T}} P_0 \tilde{\mathrm{f}} + \tilde{\mathrm{f}}^{\mathrm{T}} P_0 \tilde{\dot{\mathrm{f}}} \\
&= e^{\mathrm{T}} \left(A_0{}^{\mathrm{T}} P + P A_0\right) e + 2 e^{\mathrm{T}} P D (v - d(x,u,t)) \\
&\quad + 2 e^{\mathrm{T}} P G \tilde{\mathrm{f}} + 2 \tilde{\dot{\mathrm{f}}}^{\mathrm{T}} P_0 \tilde{\mathrm{f}} \\
&= -e^{T} Q e + 2 e^{\mathrm{T}} \underbrace{P D}_{P} \left(-\rho \frac{F e}{\|F e\|} - d(x,u,t)\right) \\
&\quad + 2 \left(e^{\mathrm{T}} P G + \tilde{\dot{\mathrm{f}}}^{\mathrm{T}} P_0\right) \tilde{\mathrm{f}} \\
&\leqslant -e^{T} Q e + 2 \left(e^{\mathrm{T}} P G + \tilde{\dot{\mathrm{f}}}^{\mathrm{T}} P_0\right) \tilde{\mathrm{f}} \\
\tilde{\dot{\mathrm{f}}} &= -P_0^{-1} G^{\mathrm{T}} P e \Rightarrow \dot{V} \leqslant 0.
\end{aligned} \tag{13}$$

□

Remark 1. Since the fault detected in this paper is an extreme case that a complete failure occurs on the DPSA, the fault signal f only has five states as 0/−1/−2/−3/−4, which will act like a step signal if the fault occurs. The derivative of the fault signal f will be zero except at the moment the fault occurred, which is such a high value that will influence the effect of the fault detector and FTC. Hence, the fault reconstruction law designed is as follows, which neglects the effects of the $\dot{\mathrm{f}}$:

$$\begin{aligned}
\hat{\mathrm{f}} &= \tilde{\dot{\mathrm{f}}} + \dot{\mathrm{f}} = \tilde{\dot{\mathrm{f}}} \\
&= -P_0^{-1} G^{\mathrm{T}} P e.
\end{aligned} \tag{14}$$

It is notable that according to (1), the fault distribution matrix $G = \left(\begin{smallmatrix} 0 \\ \frac{k(du-h)}{mn} \end{smallmatrix}\right)$. To realize the assumption 3, C must be $\left(\begin{smallmatrix} 1 & 0 \\ 0 & 1 \end{smallmatrix}\right)$. Hence, in practical experiments, the velocity of the DPSA needs to be indirectly measured. According to the parameters identified by the open-loop test, as shown in table 1, the observer gain matrix is designed as $L = \left(\begin{smallmatrix} 2 & 0 \\ 0 & 1 \end{smallmatrix}\right)$, then the eigenvalues of matrix A_0 are as follows:

$$\begin{aligned}
\lambda_1 &= -6.8 \times 10^3 + 5.98 \times 10^3 i, \\
\lambda_2 &= -6.8 \times 10^3 - 5.98 \times 10^3 i
\end{aligned} \tag{15}$$

which is satisfied with assumption 1.

the Lyapunov matrix pair (P,Q) is designed for the fault detector with SMO:

$$\begin{aligned}
Q &= \begin{pmatrix} 6 & -3 \\ -3 & 2 \end{pmatrix}; Q = A_0^{\mathrm{T}} P + P A_0 \Rightarrow \\
P &= \begin{pmatrix} 6 \times 10^3 & -1.4 \times 10^{-4} \\ -1.4 \times 10^{-4} & 7.3 \times 10^{-5} \end{pmatrix}; P_0 = 1 \times 10^5.
\end{aligned} \tag{16}$$

Then the eigenvalues of matrices P, Q are as follows:

$$\begin{aligned}
\text{Eigenvalue of } P &: \lambda_1 = 7.3 \times 10^{-5},\ \lambda_2 = 6.0 \times 10^3 \\
\text{Eigenvalue of } Q &: \lambda_1 = 0.4,\ \lambda_2 = 7.6
\end{aligned} \tag{17}$$

which is satisfied with assumption 2. Based on the above design, the assumptions 1∼3 are satisfied. The ρ is determined through the trial and error method by experiments. The relationships between the ρ and the fault detector's accuracy and speed are also discussed in sections 5 and 6.

4. FTC strategy

4.1. The overall design of FTC

With the designed structure of the DPSA and the fault detector with SMO, the FTC strategy can be designed. As shown in figure 6(a), the scheme of the FTC uses the fault detector to automatically reconstruct the fault signal f and detect the failures of the DPSA. The tracking controller is added to realize the trajectory tracking. With the detection results from the fault detector, the on/off status of the spare-PSLs can be updated thus realizing the control reallocation.

Since the inputs of the SMO are (1) output displacement of the DPSA signal; (2) control force of the DPSA u_{fb}; (3) velocity of the DPSA. Here, the velocity needs to be indirectly measured by taking the derivative of the displacement signal. To avoid the negative effects of the measurement noise on the velocity calculation, a low-pass filter is added in the loop, the bandwidth of which is set to reject the noise as well as higher than the operating frequency of the DPSA.

To realize the trajectory tracking of DPSA, the tracking controller adopted here is an integral controller that is widely used to provide high-gain feedback and overcome creep and vibrations in systems suffering from hysteresis at relatively low frequencies [39].

The supervisory loop of the FTC consists of two groups of fault detectors, which are explained in the next subsection.

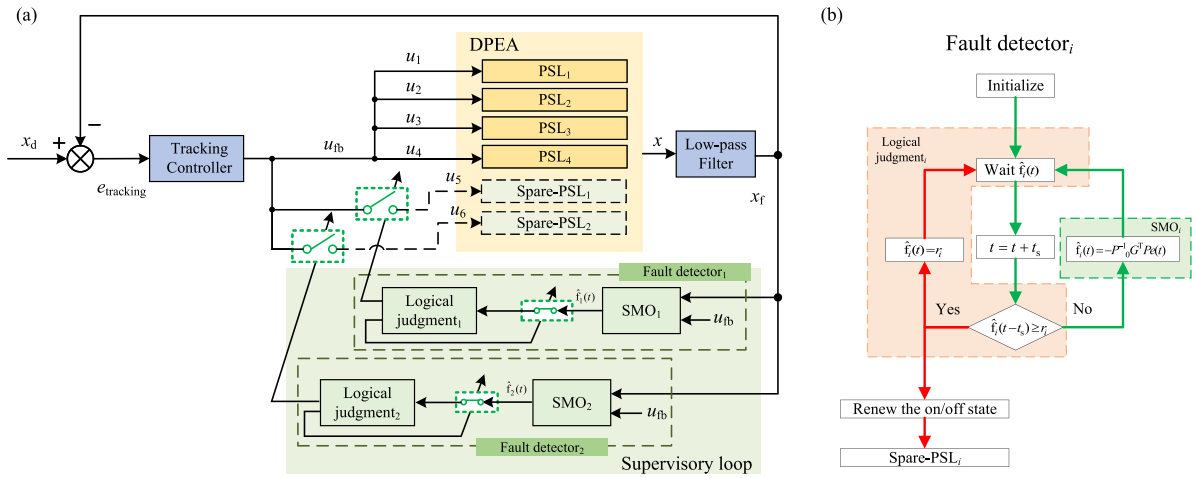

Figure 6. Fault-torlerant control strategy diagram: (a) overall FTC strategy diagram. (b) Flowchart of the fault detector design for decision-making.

4.2. The design of the supervisory loop of FTC

To incorporate a SMO into the FTC loop, it is necessary not only to achieve the observation of fault signal but also to implement the control reallocation on the redundant hardware resources. Hence, two groups of SMO-based fault detectors along with logical judgments are designed in the supervisory loop. The flowchart of the fault detector design for decision-making is illustrated in figure 6(b).

The SMO of each fault detector is designed in section 3. The logical judgment of each fault detector is to make a comparison between the estimated fault signal $\hat{\mathrm{f}}$ from SMO and the thresholds specified, thus renewing the on/off state of the spare-PSL if the fault is detected. The thresholds are designed as follows:

$$\tilde{\mathrm{f}}_{\max} > r_{\mathrm{f1}} > r_{\mathrm{f2}} \geqslant -1 \tag{18}$$

where $r_{\mathrm{f}i}$ represents the threshold set for the logical judgment i, $\tilde{\mathrm{f}}_{\max}$ means the maximum error between the estimated value $\hat{\mathrm{f}}$ and the actual value f.

Remark 2. Here $\tilde{\mathrm{f}}_{\max} > r_{\mathrm{f}i} \geqslant -1$ is set for avoiding misdiagnosis caused by the observational errors. In practice, the maximum error between the estimated value $\hat{\mathrm{f}}$ and the actual value f can be obtained under the occasion that no fault takes place.

Remark 3. Here $r_{\mathrm{f1}} > r_{\mathrm{f2}}$ is set if one PSL breaks down, the fault detector$_1$ will take effect quicker than the PSL$_2$ and the estimated fault signal $\hat{\mathrm{f}}$ can then increase because of the spare-PSL$_1$ outputs the displacement. Thus the fault detector$_2$ will not send out the command signal to actuate the spare-PSL$_2$ until another PSL breaks down.

Remark 4. If the SMO$_i$ has detected the fault of one PSL, the estimated results of it will be kept as the final valuer_{fi}, thus the spare-PSL controlled by this group of fault detectors will be actuated until it breaks down. The state preservation above can be achieved through the design of sign functions and integration.

Hence, the overall control force to actuate the DPSA can be got as follows:

$$\begin{cases} U(t) = [u_1(t), u_2(t), \ldots u_6(t)]^T = k_{\mathrm{i}} e_{\mathrm{tracking}}(t) \begin{bmatrix} I_{4\times 1} \\ S(t)_{2\times 1} \end{bmatrix} \\ S = \begin{bmatrix} s_1(t) \\ s_2(t) \end{bmatrix} = \begin{bmatrix} \hat{\mathrm{f}}_1(t-t_{\mathrm{s}}) + \mathrm{sgn}\left\{ \max\left[\int_0^t \max\left(r_{\mathrm{f1}} - \hat{\mathrm{f}}_1(t-t_{\mathrm{s}}), 0 \right) \mathrm{d}t, 0 \right] \right\} \left(r_{\mathrm{f1}} - \hat{\mathrm{f}}_1(t-t_{\mathrm{s}}) \right) \\ \hat{\mathrm{f}}_2(t-t_{\mathrm{s}}) + \mathrm{sgn}\left\{ \max\left[\int_0^t \max\left(r_{\mathrm{f2}} - \hat{\mathrm{f}}_2(t-t_{\mathrm{s}}), 0 \right) \mathrm{d}t, 0 \right] \right\} \left(r_{\mathrm{f2}} - \hat{\mathrm{f}}_2(t-t_{\mathrm{s}}) \right) \end{bmatrix} \end{cases} \tag{19}$$

where the u_i is the control force of PSL_i, $e_{tracking}$ is the tracking error. k_i is the integral parameter of the tracking controller, t_s is the sampling time.

5. Experimental evaluations

In the experiments, faults in DPSA are not induced by extreme operating conditions to simulate genuine piezoelectric breakdown faults. Instead, during actuator operation, the exciting voltage of one PSL is manually set to zero to approximate real failure conditions. The abilities of the designed fault detector to detect faults through displacement signals and FTC's control force reallocation are solely concerned with.

5.1. Performance verification of the SMO-based fault detector

To validate the feasibility and performance of the proposed SMO-based fault detector, experiments are designed to examine different fault cases. Meanwhile, the relationship between the ρ and the accuracy of the fault detector is studied based on the fault detector results. The parameters used in the experiments include (i) ρ, F, δ of SMO, (ii) the cut-off frequency of the low-pass filter shown in table 2, and (iii) parameters of the DPSA mathematical model shown in table 1.

Fault case 1: for the purpose of testing the performance of the fault detector under different displacement amplitudes, this fault case is conducted with varying ρ and fault occurrence times while maintaining a constant signal frequency. Only one PSL breaks down and the faulty PSL is randomly selected.

As depicted in figure 7, type 1 is that fault occurs at the moment of maximum output displacement. In contrast, type 2 represents the fault that arises at the minimum output displacement. These specific fault scenarios assess the fault detector's capability to detect faults regardless of when they occur. The input voltage is the sinusoidal signal of 1 Hz from 0 to 100 V (peak-to-peak magnitude). Hence, the displacement of DPSA is also 1 Hz. Three conclusions can be obtained from the experimental results in figure 7:

(1) The proposed SMO-based fault detector can reconstruct the displacement and fault signal f accurately under low-speed (1 Hz) conditions.
(2) Increasing the ρ value can accelerate the speed of fault reconstruction and improve the accuracy of displacement value observation. However, when there are certain unmodeled errors, a too large ρ value can cause the observer to reduce the observation error of the displacement by correcting the saturation function v. This will lead to a rapid change in the estimated fault signal $\hat{f}$, as figure 7(c) shows and pose a risk of misdiagnosis.
(3) It is necessary to choose a suitable ρ value to ensure both the speed of fault reconstruction and the reduction of misdiagnosis rates and then meet the requirements of FTC. In this case, $\rho = 1000$ is a more suitable choice.

Fault case 2: for the purpose of testing the performance of the fault detector under different working frequencies, this fault case is conducted with varying ρ and signal frequency while only one PSL breaks down at a constant fault occurrence time. Here, the faulty PSL and fault occurrence time are randomly generated.

As figure 8 shows, type $1-3$ respectively are the conditions that fault occurs when the output displacement signal's frequency is different. Here, the input voltage is the sinusoidal signal of 1 Hz, 5 Hz, and 10 Hz and from 0 to 100 V (peak-to-peak magnitude).

Figures 8(a) and (d) are the results of type 1: the faulty PSL is the PSL_4, with fault occurrence time at 4.183 s. Figures 8(b) and (e) are the results of type 2: the faulty PSL is the PSL_4, with fault occurrence time at 0.471 s. Figures 8(c) and (f) are the results of type 3: the faulty PSLs are the PSL_3, with fault occurrence time at 0.378 s. Three conclusions can be obtained from figure 8:

(1) The proposed SMO-based fault detector can estimate the displacement and fault signal f accurately under low-speed (1 Hz) conditions.
(2) As the frequency of the observation signal increases, a too low ρ value results in inadequate fault reconstruction speed and can lead to misdiagnosis. It is necessary to select an appropriate ρ value to ensure both the speed of fault reconstruction and the reduction of misdiagnosis rates meet the requirements of FTC.
(3) For FTC demands, when the observation signal frequency is 1 Hz, $\rho = 1000$; when it is 5 Hz, $\rho = 5000$; and when it is 10 Hz, $\rho = 10000$ are more suitable.

Fault case 3: for the purpose of testing if fault detector can detect the fault when several PSLs break down, a more general fault case is designed for validation: fault takes place on two PSLs, while the fault occurrence time and faulty PSLs are randomly generated. Furthermore, the input voltage is the sinusoidal signal of 1 Hz, 5 Hz, and 10 Hz and from 0 to 100 V (peak-to-peak magnitude) to validate the fault detector's performance under different working frequencies.

Figures 9(a) and (d) are the results of type 1: the faulty PSLs are the PSL_1 and PSL_4, with fault occurrence time at 1.40 s and 4.08 s respectively.

Figures 9(b) and (e) are the results of type 2: the faulty PSLs are the PSL_3 and PSL_4, with fault occurrence time at 0.49 s and 0.87 s respectively.

Figures 9(c) and (f) are the results of type 3: the faulty PSLs are the PSL_1 and PSL_2, with fault occurrence time at 0.039 s and 0.019 s respectively. Furthermore, unlike the other types, the fault occurrence time of the two faulty PSLs is so close that this type can describe the fault detector performance when multiple PSLs break down simultaneously.

As figures 9(d)–(f) shows, the fault detector can estimate the number of fault layers: if there is one fault layer, the estimated f value is -1, and if there are two fault layers, it is -2. Hence, the conclusion can be drawn that the proposed SMO-based fault detector can estimate the displacement and fault signal f accurately under different working frequencies, faulty PSL numbers, fault occurrence times, and faulty PSLs.

Table 2. Parameters used in the experiments.

Experiment	Param.	Value
Fault detector	ρ	1000 (1 Hz) 5000 (5 Hz) 10 000 (10 Hz)
	F	1
	δ	0.5
	Cut-off frequency	1000 Hz
FTC	ρ	1000 (1 Hz) 5000 (5 Hz) 10 000 (10 Hz)
	F	1
	δ	0.5
	Cut-off frequency	1000 Hz
	r_1	0.8
	r_2	0.9
	k_i	300

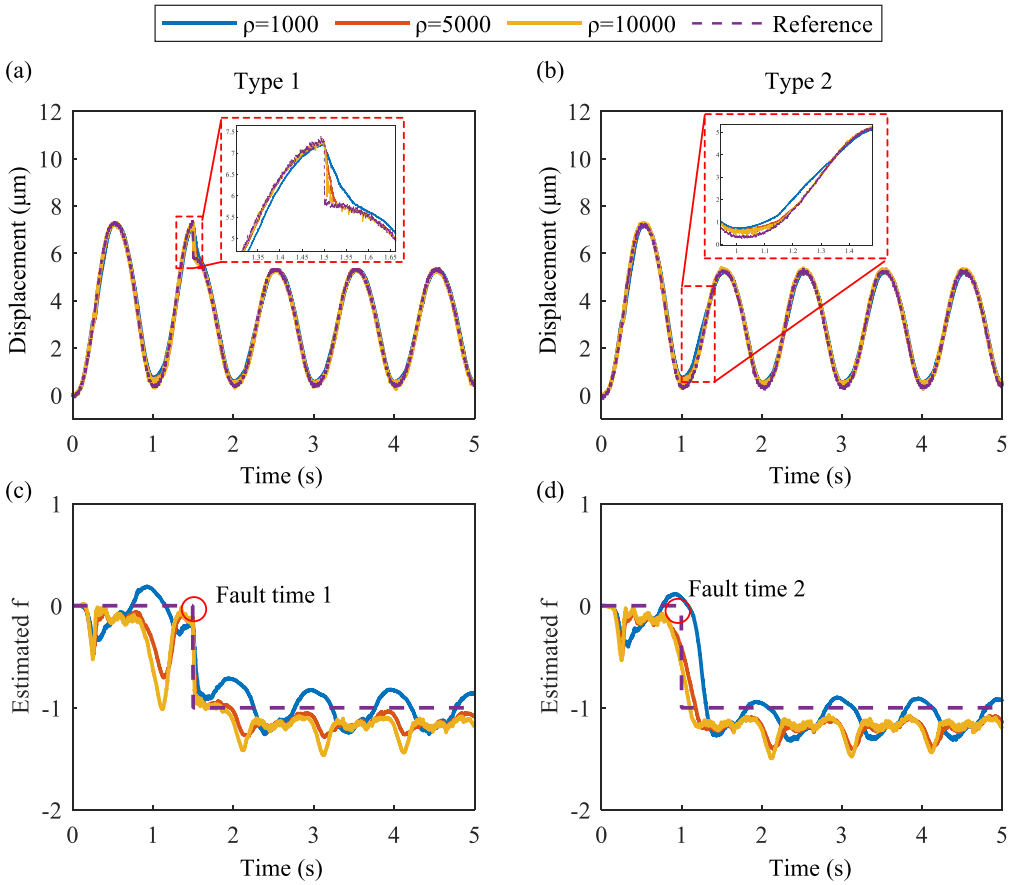

Figure 7. The fault detector reconstruction performance of the **Fault case 1**. (a) Displacement reconstruction under type 1. (b) Displacement reconstruction under type 2. (c) Fault signal f reconstruction under the type 1. (d) Fault signal f reconstruction under the type 2.

5.2. Performance verification of the FTC

To validate the feasibility and performance of the proposed FTC, experiments with different fault cases are designed. Since the fault occurs on the condition that the DPSA is tracking trajectory, the reference signal should be designed first. The full-scale displacement of the DPSA with four PSLs is 7 μm under 100 V. It is noticeable that a positive offset of the tracking signal needs to be set to avoid the negative control force to be generated and damage the DPSA. Hence, the tracking references of the FTC verification are sinusoidal signals from 1 to 10 Hz and from 0 to 2 μm (peak-to-peak magnitude with an offset of 4 μm), as figures 10(a)–(c) show. The parameters used in the experiments include (i) ρ, F, δ of SMO, (ii) the cut-off frequency of the low-pass filter, (iii) the coefficient k_i of the integral controller coefficient, (iv) the threshold set r_i for the logical judgment, which are all shown in table 2,

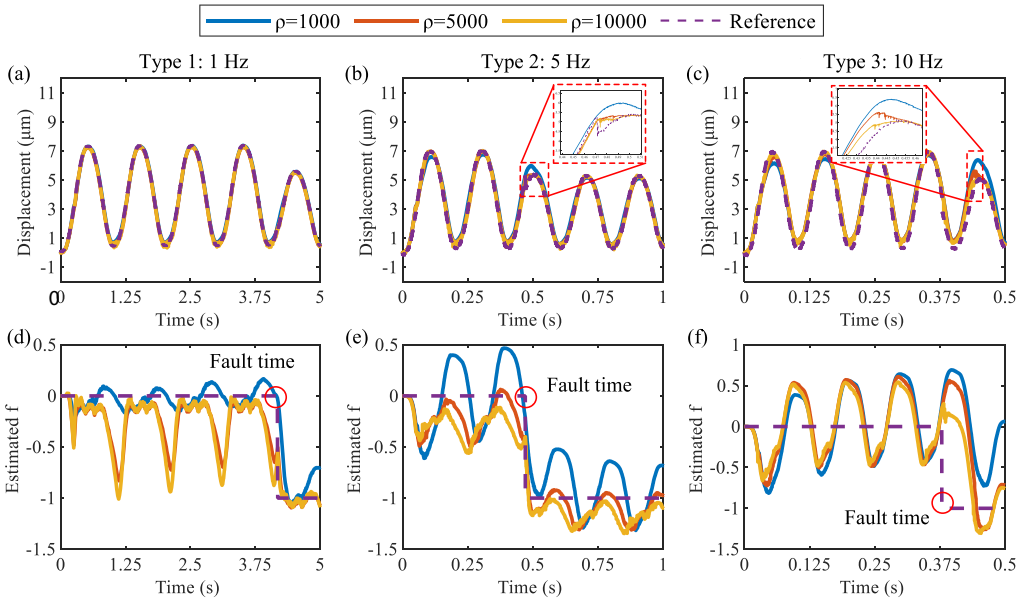

Figure 8. The fault detector reconstruction performance of the **Fault case 2**. (a) Displacement reconstruction under type 1. (b) Displacement reconstruction under type 2. (c) Displacement reconstruction under type 3. (d) Fault signal f reconstruction under the type 1. (e) Fault signal f reconstruction under the type 2. (f) Fault signal f reconstruction under the type 3.

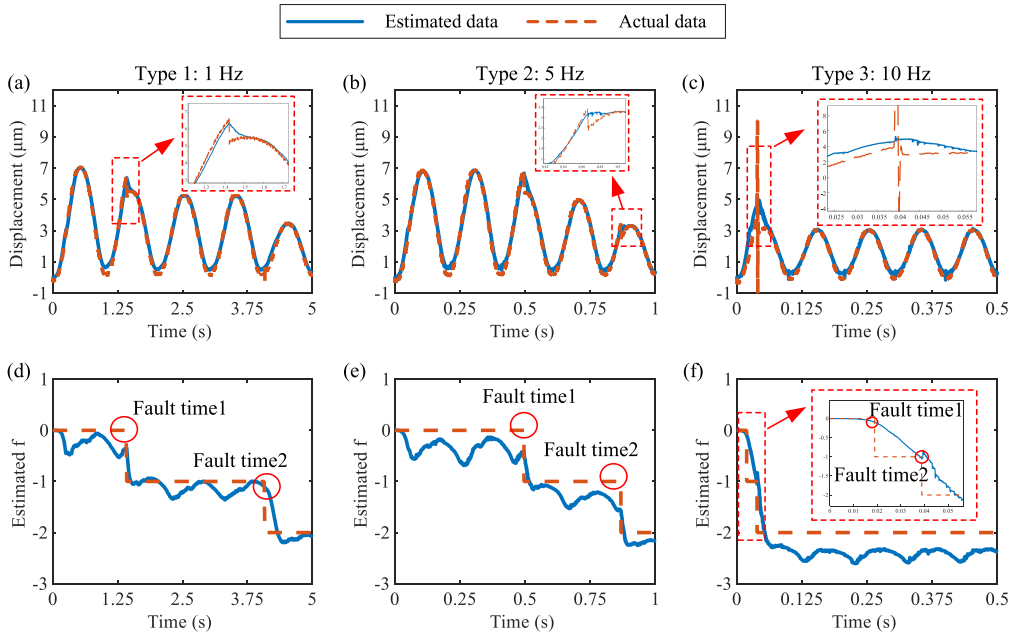

Figure 9. The fault detector reconstruction performance of the **Fault case 3**. (a) Displacement reconstruction under type 1. (b) Displacement reconstruction under type 2. (c) Displacement reconstruction under type 3. (d) Fault signal f reconstruction under the type 1. (e) Fault signal f reconstruction under the type 2. (f) Fault signal f reconstruction under the type 3.

and (v) parameters of the DPSA mathematical model shown in table 1.

Fault case 1: For the purpose of testing if the fault tolerant control can realize the control force allocation under different working frequencies, this paper chooses the value ranging from 1–10 Hz, which is within the closed-loop bandwidth. In this case, only one PSL breaks down while the DPSA works, while the fault occurrence time and faulty PSL are randomly generated. The tracking and fault-tolerance cases can be found in figure 10.

Figures 10(a) and (d) are the results while the reference signal is 1 Hz so that the ρ value is set as 1000. The faulty PSL is the PSL_4, with fault occurrence time at 2.48 s. Without FTC, the displacement of the DPSA (blue solid line in figure 10(a)) is restricted because the maximum value of the control force

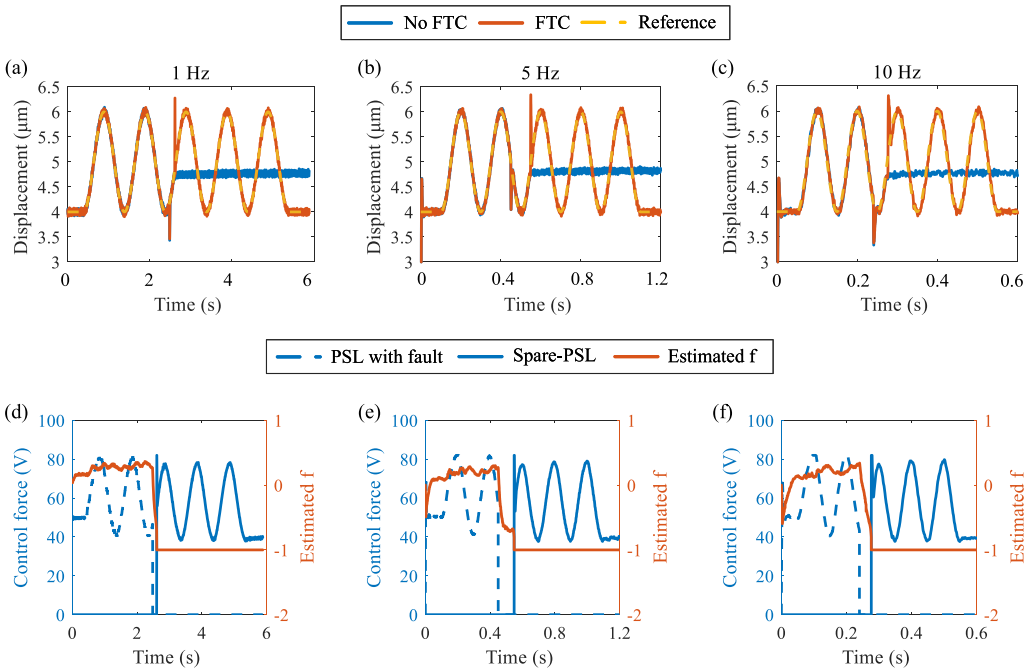

Figure 10. Comparative tracking results of sinusoidal references with the FTC of **Fault case 1**. (a)–(c) Output displacements for 1, 5, and 10 Hz, respectively. (d)–(f) Control force and estimated f of different PSLs for 1, 5, and 10 Hz, respectively.

Table 3. Experimental results of statistical tracking errors of **Fault case 1**.

	No FTC		With FTC	
Frequency (Hz)	e_{rms} (μm)	$e_{\max}$ (μm)	e_{rms} (μm)	$e_{\max}$ (μm)
1	0.572	0.862	0.044	1.400
5	0.580	0.900	0.027	1.333
10	0.603	0.821	0.232	1.119

is limited under 82 V to prevent the overload input voltage from bringing damage to the PSLs. With the FTC, the control force begins to actuate the spare-PSL_1 (blue solid line in figure 10(d)) when the fault detector has detected the fault signal f (orange solid line in figure 10(d)).

Similar results of the FTC under different working frequencies can be found in other subgraphs of figure 10. It can be concluded that the FTC with double-PSL (yellow solid line in figures 10(a)–(c)) can realize the trajectory tracking and control reallocation in experiments.

To further quantify tracking errors, the RMS error (e_{rms}) and the maximum error($e_{\max}$) are calculated in this paper, as table 3 shows.

The specific improvement ratio is given that: in comparison with no FTC, the RMS error with FTC can be reduced by 92% (1 Hz), 95% (5 Hz) and 61% (10 Hz). Under 10 Hz, the effect of FTC decreased since the closed-loop bandwidth. The maximum error with FTC is larger than the one without FTC because if the control force is reallocated to the spare-PSLs, an overshoot of PSLs' output displacement will occur.

Fault case 2: for the purpose of testing if the FTC can realize the control force allocation when several PSLs break down, this case is used to test if two SPLs break down while the DPSA is working, which is the maximum number of the spare-PSLs in this paper. The fault occurrence time and faulty PSLs are randomly generated. The tracking and fault-tolerance cases can be found in figure 11.

Figures 11(a) and (d) are the results while the reference is 1 Hz: the faulty PSLs are the PSL_3 and PSL_4, with the fault occurrence time at 2.28 s and 4.18 s respectively.

Without FTC or FTC with single-PSL, the displacement of the DPSA (blue and orange solid line in figure 10(a)) is restricted because the maximum value of the control force's value is limited under 82 V to prevent the overload input voltage breaking the PSLs. Hence, if two PSLs break down, double-PSL (spare-PSL_1 and spare-PSL_2) is needed for the FTC.

When the FTC with double-PSL is applied, the fault detector$_1$ with SMO_1 first detects fault signal f (blue solid line in figure 11(g)). At this moment, the control force begins to actuate the spare-PSL_1 (blue solid line in figure 11(d)) and the estimated fault signal $\hat{f}$ of SMO_1 is kept as -1, thus the supervisory loop with SMO_1 loses effect. When the other PSL breaks down, the supervisory loop with SMO_2 detects fault signal f (orange solid line in figure 11(g)). Then the control force begins to actuate the spare-PSL_2 (orange solid line in

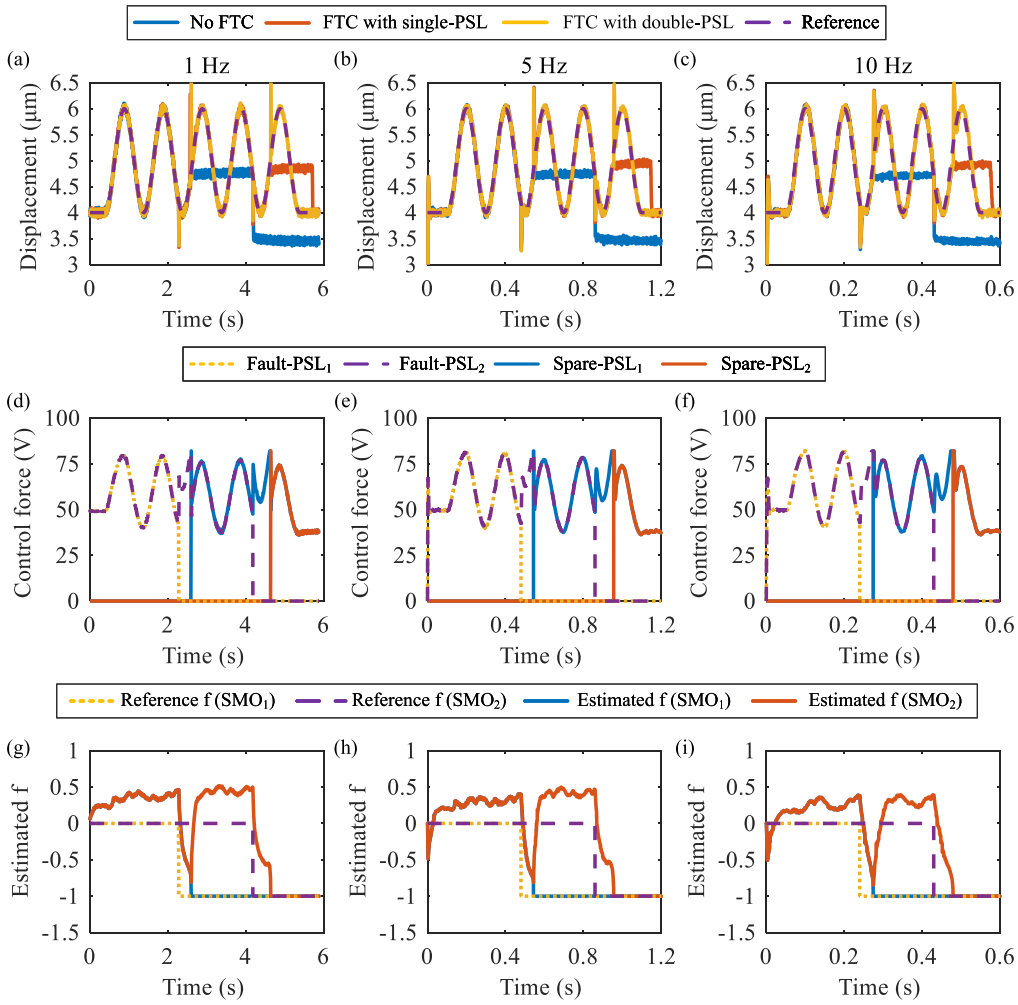

Figure 11. Comparative tracking results of sinusoidal references with the FTC of **Fault case 2**. (a)–(c) Output displacements for 1, 5, and 10 Hz, respectively. (d)–(f) Control force of different PSLs for 1, 5, and 10 Hz, respectively. (g)–(f) Estimated fault signal f for 1, 5, and 10 Hz, respectively.

Table 4. Experimental results of statistical tracking errors of **Fault case 2**.

	No FTC		With FTC	
Frequency (Hz)	e_{rms} (μm)	$e_{\max}$ (μm)	e_{rms} (μm)	$e_{\max}$ (μm)
1	0.837	0.813	0.058	1.697
5	0.841	0.808	0.178	1.526
10	0.866	0.749	0.248	1.270

figure 11(d)). The estimated fault signal $\hat{\text{f}}$ of SMO_2 is also kept as -1, thus the supervisory loop with SMO_2 loses effect.

Similar results of the FTC under different working frequencies can be found in other subgraphs of figure 11. It can be concluded that the FTC with double-PSL (yellow solid line in figures 11(a)–(c)) can realize the trajectory tracking and control reallocation in experiments.

In Fault case 2, the RMS error (e_{rms}) and the maximum error ($e_{\max}$) are also calculated, as table 4 shows. The specific improvement ratio is given that: in comparison with no FTC, the RMS error with FTC can be reduced by 93% (1 Hz), 78% (5 Hz) and 71% (10 Hz).

6. Discussion

In this section, discussions are made considering the experimental results of the SMO-based fault detector and the FTC.

6.1. Performance of fault detector

The above analysis of experimental results is mainly conducted through the different fault cases which are predesigned. The key of the fault detector is to realize the reconstruction of the fault signal f. Based on the estimated results from the SMO, it can be found that the proposed SMO-based fault detector

can reconstruct the displacement and fault signal f accurately under different working frequencies (1–10 Hz), faulty PSL numbers, fault occurrence times, and faulty PSLs. It is notable that in experiments of fault detector, the ρ of SMO is the only parameter necessary to select. With the variation of the working frequency, an appropriate ρ value ensures both the speed of fault reconstruction and the reduction of misdiagnosis rates.

6.2. Performance of FTC

For active FTC, it can be revealed from the experimental observations that based on the spare-PSLs of DPSA, the FTC realizes (i) control reallocation after the supervisory loop makes a decision and (ii) trajectory tracking under different working frequencies (1–10 Hz), faulty PSL numbers, fault occurrence times, and faulty PSLs. The maximum compensation displacement accuracy in this paper is with the RMS error of 0.027 μm (5 Hz, 0–6 μm) under fault case 1. It is notable that in this work, there are two SMO-based fault detectors in the supervisory loop of FTC, corresponding to the two spare-PSLs respectively. If more spare-PSLs are added to the DPSA, the fault detectors should also be increased. Hence, redundant resources and elements are a must for breakdown failure. Reliability and cost are contradictory to each other. Improving reliability often brings about the disadvantage of increased costs.

6.3. Challenges and future directions

The proposed DPSA and its FTC strategy are attractive for applications mainly due to (i) complete fault of the PSA; (ii) state estimation and fault reconstruction of PSA; (iii) robustness to unknown uncertainty or unmodeled error. To be honest, there is also a shortcoming in the proposed SMO-based fault detector and FTC, i.e. the ρ value is selected manually in different working frequencies. If the ρ value is too small, the speed of fault reconstruction cannot be guaranteed. If the ρ value is too large, the observation error $\tilde{f}$ will be large thus causing the misdiagnosis. Hence, the proposed SMO-based fault detector and FTC can be improved further by combining them with some adaptive methods to renew the ρ value for different working frequencies. However, this is not the emphasis of this work.

7. Conclusions

In this paper, a novel DPSA structure with redundant PSLs is proposed for the active FTC to improve the PEA's reliability. Based on the DPSA mathematical model with fault, inherent nonlinearity, and unknown uncertainty, The SMO-based fault detector is designed to reconstruct the fault. With the above work, the FTC strategy is proposed with a supervisory loop consisting of two groups of SMO-based fault detectors. An integral controller is applied for trajectory tracking of DPSA. Experimental results have verified a promising fault reconstruction performance of the fault detector and the effectiveness of the proposed FTC strategy with DPSA under various fault cases. The significance of this work lies in that it not only provides a new structure and working principle of PSA systems but also includes rigorous theoretical support for fault detection and FTC to improve the PSA's reliability in practice. The new structure can be easily extended to all the PSA systems, while the proposed SMO-based fault detector is suitable for most PEAs. It is worth noting that the ρ value in the current design can be optimized using other adaptive or optimal methods. In addition, the working bandwidth of the DPSA and FTC should be broadened in future work.

Data availability statement

No new data were created or analysed in this study.

Acknowledgments

This work was supported by the Fundamental Research Funds for the Central Universities (Grant No. NS2022051).

ORCID iDs

Yunzhi Zhang https://orcid.org/0009-0000-7460-2272
Jie Ling https://orcid.org/0000-0002-6786-0422
Yuchuan Zhu https://orcid.org/0000-0002-7399-1656

References

[1] Ling J, Chen L, Feng Z and Zhu Y 2022 *Mech. Mach. Theory* **176** 104997
[2] Duan Y, Peng H, Zhu Y, Shen Y and Ling J 2023 *2023 IEEE Int. Conf. on Robotics and Biomimetics (ROBIO)* pp 1–6
[3] Wang B, Du Y and Ye Z 2020 *IEEE/ASME Trans. Mechatronics* **25** 848–58
[4] Ling J, Chen L, Zhang M and Zhu Y 2023 *Smart Mater. Struct.* **32** 025011
[5] Tamburrano P, Sciatti F, Plummer A R, Distaso E, De Palma P and Amirante R 2021 *Energies* **14** 4858
[6] Ling M, He X, Wu M and Cao L 2022 *IEEE/ASME Trans. Mechatronics* **27** 4942–50
[7] Yu J, Jiao Z and Wu S 2020 *J. Mech. Eng.* **56** 226–34
[8] Simic M and Herakovic N 2021 *J. Clean. Prod.* **284** 124748
[9] Guo Y, Zhu Y, Li Y, Fei S, Zhu B, Zhang X and Wang X 2018 *J. Intell. Mater. Syst. Struct.* **29** 1348–59
[10] Senousy M, Rajapakse R, Mumford D and Gadala M 2009 *Smart Mater. Struct.* **18** 045008
[11] Huang C, Cai K, Wang Y, Bai Y and Guo D 2018 *J. Mater. Chem.* **6** 1433–44
[12] Peddigari M, Kwak M S, Min Y, Ahn C W, Choi J J, Hahn B D, Choi C, Hwang G T, Yoon W H and Jang J 2021 *Nano Energy* **88** 106279
[13] Zhang S, Lee H J, Jiang X, Huang W, Sherrit S and Kropf M M 2016 *Low Temperature Materials and Mechanisms* (CRC Press) pp 201–30
[14] Ramesh R, Kumar R K and Kumar T V 2013 *J. Electroceram.* **30** 251–7
[15] Stewart M and Cain M G 2014 *Characterisation of Ferroelectric Bulk Materials and Thin Films* (Springer) pp 147–89
[16] Chaplya P M, Mitrovic M, Carman G P and Straub F K 2006 *J. Appl. Phys.* **100** 124111
[17] Alwi H, Edwards C and Tan C P 2011 *Fault Detection and Fault-Tolerant Control Using Sliding Modes* (Springer)

[18] Frank P M 1990 *Automatica* **26** 459–74
[19] Gao Z, Ding S X and Cecati C 2015 *IEEE Trans. Ind. Electron.* **62** 3752–6
[20] Ding S X 2008 *Model-Based Fault Diagnosis Techniques: Design Schemes, Algorithms and Tools* (Springer)
[21] Edwards C and Spurgeon S 1998 *Sliding Mode Control: Theory and Applications* (CRC Press)
[22] Utkin V I 2013 *Sliding Modes in Control and Optimization* (Springer)
[23] Sreedhar R, Fernandez B and Masada G 1993 *Proc. IEEE Int. Conf. on Control and Applications* pp 715–21
[24] Tan C P and Edwards C 2003 *Int. J. Robust Nonlinear Control IFAC Affiliated J.* **13** 443–63
[25] Yan X and Edwards C 2007 *Int. J. Adapt. Control Signal Process.* **21** 657–73
[26] Edwards C, Alwi H and Menon P P 2013 *Applications of Sliding Observers for FDI in Aerospace Systems* (Springer) pp 341–60
[27] Su X, Liu X and Song Y D 2018 *IEEE/ASME Trans. Mechatronics* **23** 38–47
[28] Gou L, Shen Y, Zheng H and Zeng X 2020 *IEEE Access* **8** 10186–97
[29] Chen L, Edwards C, Alwi H and Sato M 2019 *American Control Conf. (ACC)* pp 4436–41
[30] Gu G, Zhu L M, Su C Y, Ding H and Fatikow S 2014 *IEEE Trans. Autom. Sci. Eng.* **13** 313–32
[31] Gan J and Zhang X 2019 *AIP Adv.* **9** 040702
[32] Peng J Y and Chen X B 2012 *IEEE/ASME Trans. Mechatronics* **19** 88–99
[33] Zhang Y and Yan P 2016 *Smart Mater. Struct.* **25** 125011
[34] Yan X G and Edwards C 2007 *Automatica* **43** 1605–14
[35] He J and Zhang C 2012 *Math. Probl. Eng.* **2012** 451843
[36] Yu Y and Dong Y 2019 *Int. J. Aerosp. Eng.* **2019** 1–12
[37] Ling J, Feng Z, Zheng D, Yang J, Yu H and Xiao X 2021 *Mech. Syst. Signal Process.* **150** 107235
[38] Macki J W, Nistri P and Zecca P 1993 *SIAM Rev.* **35** 94–123
[39] Hassani V, Tjahjowidodo T and Do T N 2014 *Mech. Syst. Signal Process.* **49** 209–33